Mutual inductance surrogate model of the UWPT system and its constant power optimization at misaligned positions

Yuchen Feng, Yue Sun[*], Tao Lin, Hongsheng Hu and Fengwei Chen

School of Automation, Chongqing University, Chongqing 400044, China
* Corresponding author, E-mail: syue@cqu.edu.cn

Abstract

Recent studies have focused on developing underwater wireless power transfer (UWPT) anti-misalignment methods to address the vulnerability of UWPT systems to large water flow fluctuations and unstable power transference. Autonomous underwater vehicles (AUVs) use irregular coupling mechanisms to ensure stable power transmission through constant mutual inductance, but these require complex structures and present docking difficulties. A prediction algorithm based on the mutual inductance surrogate model is proposed to achieve optimal prediction for coupling mechanisms with constant power transmission at misaligned positions. The relative position and posture parameters of a coupling mechanism simulation model were subjected to Latin hypercube sampling to construct a dataset. Subsequently, a back propagation (BP) neural network was applied to develop an omnidirectional surrogate coupling mechanism model to predict the mutual inductance value. The surrogate model and a genetic algorithm were used to optimize the coil posture for maintaining constant power transfer. Experimental validation reveals that at a 0.6 aspect ratio, the system can ensure constant mutual inductance and power within a 25% omnidirectional misalignment range with an average error in mutual inductance of only 0.43%. At a 10% acceptable mutual inductance drop threshold, the anti-misalignment ranges of the system increase to 2.11 times the pre-optimization range.

Introduction

Wireless power transfer (WPT) technology has been successfully applied to consumer electronics, mobile devices, electric vehicles (EVs), and many other equipment[1–5]. With the development of marine resources and the marine economy, the scope of autonomous underwater vehicle (AUV) applications has become increasingly wide. Currently, many different types of AUVs are used in various fields, including military applications, petroleum exploration, and scientific research. The battery life is still a challenge, which can be solved using WPT technology.

Given the continuous expansion in the scope of AUV tasks, the use of conventional power supply methods has limited the scope of work and continuous working duration of such vehicles, making power supply the critical factor that determines AUV performance[6–8]. Using emerging, underwater wireless power transfer (UWPT) technology shown in Fig. 1, power can be transmitted without physical contact, enabling galvanic isolation and the elimination of mechanical wear to achieve high reliability, convenience, and safety in an underwater environment[9–11]. Underwater wireless power transfer technology provides a safe and reliable transfer method for AUV underwater power, avoiding the safety hazards caused by underwater wet plugging-unplugging, which has made UWPT a focus of research in the field of wireless power transfer[12–16].

The underwater wireless power transfer environment is influenced by factors that are not found in the atmospheric environment in terms of medium density and ocean currents. In such an environment, misalignments in the coupling mechanism can be more severe and incur greater drops in mutual inductance[17]. The mutual inductance of the coupling mechanism is closely intertwined with the output power, transfer efficiency, and other system indicators[18–24], making it necessary to introduce an anti-misalign-

ment design to ensure the stable operation of the UWPT system. Currently, anti-misalignment problems in the wireless power supplies of AUV are generally resolved using irregular coupling mechanisms such as cage, curly coil, and self-latching coupling mechanisms to attain constant mutual inductance in the coupling mechanism and ensure transfer stability. However, such solutions continue to suffer from drawbacks. The output power of the cage coupling mechanism[25,26] is linked to the relative angle of the coupling mechanism, with a 36.91% difference in the output power between the best and worst cases. The curly coil coupling mechanism[17,27] requires an additional auxiliary mechanism to fix the posture during the charging process, and self-latching coupling mechanisms[28,29] require very high docking precision, making it difficult for AUVs to achieve autonomous self-latching action underwater. Overall, the existing anti-misalignment designs used in UWPT systems sacrifice system flexibility and service life. Simultaneously, problems such as docking difficulties and structural complexities make it crucial to design a power stabilization method with a high degree of freedom.

A free-positioning omnidirectional WPT system with reticulated planar transmitters has been reported[30]. It can use a designed excitation current to generate a three-dimensional (3D) rotating magnetic field to power a receiver at any position and direction. However, as reticulated planar transmitters are large and have low transfer efficiencies (only 55.6%), it is difficult to use them in UWPT systems. New hybrid inductor-capacitor-inductor and capacitor-inductor topologies have also been proposed to resolve the power drop problems caused by the misalignment of wireless charging system coupling mechanisms in electric vehicles[31,32]. The approach utilizes the differing characteristics of the respective topologies under changes in mutual inductance to achieve constant power transfer in a system at a misaligned position; using the optimization algorithm proposed in this paper, the anti-misalignment perfor-
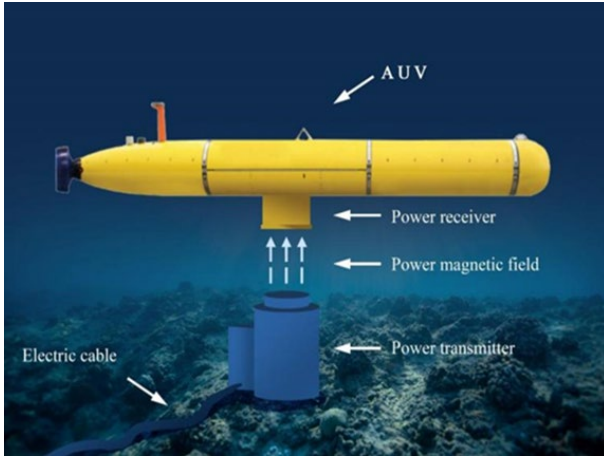
Fig. 1   Schematic of AUV wireless power transfer.

mance of UWPT systems that apply such topologies can be further improved.

This paper proposes an optimal misalignment posture prediction algorithm for coupling mechanisms based on the mutual inductance surrogate model. The proposed algorithm can attain optimal posture prediction with constant power at any position within the working range. The constant transfer of power in the misaligned state is achieved by adjusting the operating posture of the coupling mechanism. To develop the proposed method, we first established a system circuit theory model for which the mutual inductance of the system was determined as the optimization target. A back propagation (BP) neural network was then used to develop the mutual inductance surrogate model, and the optimal posture with constant power in the misaligned state was finally derived by combining the surrogate model with a genetic algorithm. The contributions of this paper are as follows:

1) An anti-misalignment method for UWPT systems based on a mutual inductance surrogate model and an optimization algorithm is proposed. The mutual inductance surrogate model developed in this study can accurately predict the mutual inductance at any position and posture of a coupling mechanism within its operating range;

2) The surrogate model and genetic algorithm were used to optimize the posture of the coupling mechanism at the misaligned position, thereby achieving constant power transfer in the system in 3D space.

AUV wireless power transfer system model and its magnetic field analysis

To determine the inputs and outputs of the mutual inductance surrogate model, this section focuses on the wireless power transfer system of an AUV with inductance and double capacitances-series (LCC-S) topology and establishes a spatial coordinate system with the geometric center of the primary coil as the origin to determine the relative position and posture parameters of its coupler. Furthermore, an in-depth analysis of the relation between mutual inductance and power transfer characteristics in the LCC-S topology are conducted. The coordinates (x, y, z) of the geometric center of the secondary coil and the rotation angles (α, β, γ) of the secondary coil around the X-, Y-, and Z-axes, respectively, are determined as the inputs of the surrogate model, with mutual inductance output determined as the output. The results provide a theoretical basis for establishing the mutual inductance surrogate model in the next section.

Relation between mutual inductance and system transfer characteristics

The LCC-S topology of an AUV wireless power transfer system is modeled and analyzed here and used to develop an equivalent circuit model. The expressions of mutual inductance and the system transfer characteristics are derived from the impedance analysis. The LCC-S circuit diagram is shown in Fig. 2. The primary side of the system in the figure comprises a DC power supply, E_{dc}, high-frequency full bridge inverters (S1–S4), and an LCC network; the secondary side of the system comprises an S network, rectifier, filter capacitor, and load resistor.

According to the theory of fundamental harmonic approximation, a DC power supply outputs a square wave through an inverter. The power supply and equivalent circuit of the inverter is represented as an AC power supply, U_I, in which R_o is the AC equivalent resistance. An equivalent circuit of this system is shown in Fig. 3, in which u_{in} and i_f represent the output voltage and output current, respectively, of the inverter and i_p indicates the current of the primary coil. The self-inductances of the primary and secondary coils of the system are L_P and L_S, respectively, and their internal resistances are R_P and R_S, respectively. L_f represents the compensation inductance at the transmitting end of the system, C_P and C_S represent the compensation capacitors in series with the primary and secondary coils of the system, respectively, C_f indicates the compensation capacitor in parallel at the transmitting end of the system, M represents the mutual inductance between the primary and secondary coils, u_o and i_o represent the input AC voltage and current of the load, respectively.

The resonance relation of the system is as follows:

$$\begin{cases} j\omega L_S + \dfrac{1}{j\omega C_S} = 0 \\[2mm] j\omega L_f + \dfrac{1}{j\omega C_f} = 0 \\[2mm] j\omega(L_P - L_f) + \dfrac{1}{j\omega C_P} = 0 \end{cases} \tag{1}$$

The impedance Z_S of the secondary side can be written as:

$$Z_S = R_S + R_O \tag{2}$$

The equivalent load R_O is given by:

$$R_O = \frac{8}{\pi^2} R_L \tag{3}$$

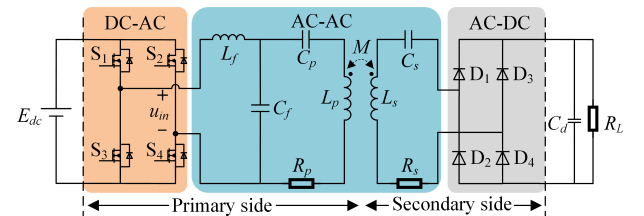The impedance Z_r reflected from the secondary side to the

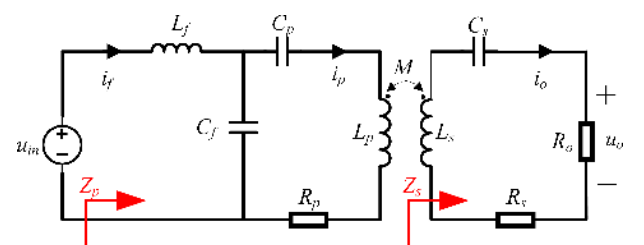**Fig. 2**   The WPT system with LCC-S compensation network.

Fig. 3   The equivalent circuit of the system.

primary side can be expressed as:

$$Z_r = \frac{(\omega M)^2}{R_S + R_O} \quad (4)$$

From this, the impedance Z_p of the primary side is:

$$Z_P = \frac{\omega^2 L_f^2 C_P (R_O + R_S)}{\omega C_P \left[\omega^2 M^2 - j\omega(L_f - L_P)(R_O + R_S) + R_P(R_O + R_S) \right] - jR_O - jR_S} \quad (5)$$

From Eqns (1) to (5), the resonant current I_f of the primary side of the system, coil current I_p of the primary side, and resonant current I_O of the secondary side can be derived as follows:

$$\begin{cases} \dot{I}_f = \dfrac{\omega C_P \left[\omega^2 M^2 - j\omega(L_f - L_P + R_P)(R_O + R_S) \right] - j(R_O + R_S)}{\omega^2 L_f^2 C_P (R_O + R_S)} \dot{U}_I \\[2mm] \dot{I}_P = \dfrac{1/j\omega C_f}{j\omega L_P + R_P + (\omega M)^2/(R_S + R_O) + 1/j\omega C_P + 1/j\omega C_f} \dot{I}_I \\[2mm] \dot{I}_O = \dfrac{j\omega M}{R_S + R_O} \dot{I}_P \end{cases} \quad (6)$$

From this, the input and output power of the system are:

$$\begin{cases} P_I = |\dot{I}_f|^2 Z_{in} = \dfrac{U_I^2 (\omega^2 M^2 + R_S R_O + R_S R_P)(R_O + R_P)}{2\omega^2 L_f^2 (R_O + R_S)^2} \\[2mm] P_O = |\dot{I}_O|^2 R_O = \dfrac{R_O U_I^2 M^2}{L_f^2 (R_O + R_S)^2} \end{cases} \quad (7)$$

The efficiency of the system can be simplified as:

$$\eta = \frac{P_O}{P_I} = \frac{\omega^2 M^2 R_O}{(\omega^2 M^2 + R_P R_O + R_S R_P)(R_O + R_S)} \times 100\% \quad (8)$$

Table 1 lists the parameters of the LCC-S topology AUV wireless power transfer system. Figure 4 shows the relation between the power, efficiency, and mutual inductance of the system. From the figure, the output power increases with the mutual inductance and the efficiency of the system increases with the mutual inductance when the inductance is small and then gradually stabilizes. Thus, the mutual inductance of the coupling coil should be increased to its maximum value to increase the output power.

The theoretical analysis above indicates that, in an LCC-S topology adopted by an AUV underwater wireless charging system, the mutual inductance is positively correlated with the transfer characteristics of the system under a constant-load scenario. Changes in mutual inductance will cause fluctuations in the transfer characteristics of the system and will have a particularly significant impact on output power.

Relation between the relative position and posture of the coupling mechanism and the mutual inductance

In the following analysis, the geometric center of the primary coil is treated as the origin of a spatial Cartesian coordinate system. In the next section, the relative position and posture of the coupling

mechanism are parameterized to facilitate the construction of a mutual inductance surrogate model.

Figure 5 shows the positional relations of the coupling mechanism of the AUV wireless power transfer system, with C_1 indicating the primary coil fixed at the charging base station and C_2 the secondary coil, which is installed on the AUV and can be rotated around its geometric center. Using the Euler angles of a rigid body rotating around a fixed point in a mechanical system[33] and considering all six degrees of freedom describing a spatial position, a 3D coordinate system can be constructed with the geometric center of the primary coil as the origin. In the figure, (x, y, z) represent the coordinates of the geometric center of the secondary coil and (α, β, γ) represent the angles through which the secondary coil rotates around the X-, Y-, and Z-axes, respectively.

According to Neumann's law, the mutual inductance between primary and secondary coils at any spatial position can be derived as

$$M = \frac{N_1 N_2 u_w}{4\pi} \oint \oint \frac{\vec{dl_1} \cdot \vec{dl_2}}{r_{12}} \quad (9)$$

where, M represents the mutual inductance between the primary and secondary coils, N_1 and N_2 indicate the number of turns in the primary and secondary coils, respectively, u_w represents the average magnetic permeability in seawater, $\vec{dl_1}$ and $\vec{dl_2}$ represent the microelements in the primary and secondary coils, respectively, and r_{12} is the geometric distance between $\vec{dl_1}$ and $\vec{dl_2}$.

The mutual inductance of the primary and secondary coils, which have relatively complex structures with multiple turns, can be established in terms of the parameters of the 3D spatial coordinate system with the origin at the geometric center of the primary coil:

$$M = f(x, y, z, \alpha, \beta, \gamma) \quad (10)$$

The relations between independent changes in each parameter and the mutual inductance are shown in Fig. 6. The initial state of
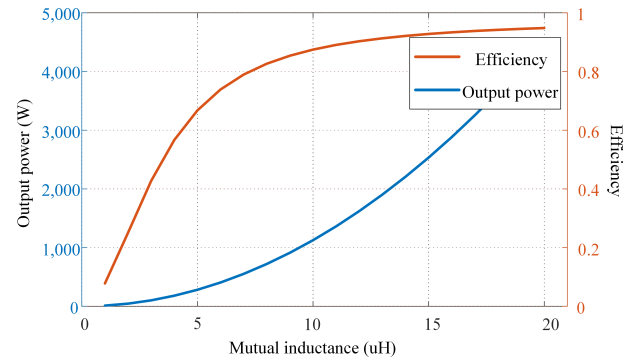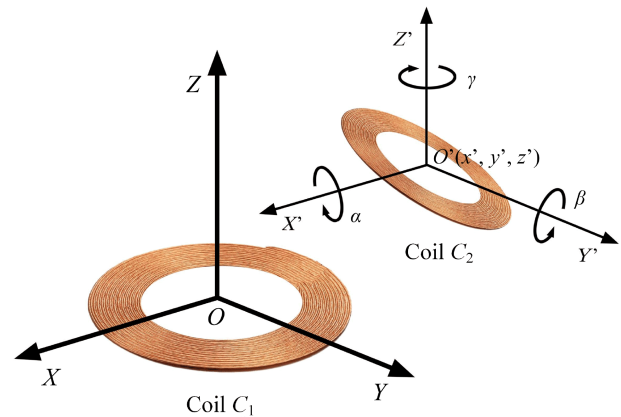

Fig. 4 Output power and efficiency.

Table 1. Coupler parameters.

Symbol	Parameter	Value
U_{in}	Input voltage	200 V
f	Frequency	150 kHz
L_f	Primary compensation inductor	13 μH
C_f	Primary compensation capacitor	86.6 nF
C_p	Primary resonance capacitor	10.46 nF
L_p	Primary side coil	120.6 μH
L_s	Secondary side coil	121.2 μH
C_s	Secondary resonance capacitor	9.29 nF
R_p	Parasitic resistance of L_p	0.48 Ω
R_s	Parasitic resistance of L_s	0.51 Ω
R_o	Resistance	20 Ω

Fig. 5 Positional relation of AUV WPT system coupling mechanism.

rotation is $x = 10$, $y = 10$, $z = 50$, $\alpha = 45°$, $\beta = 45°$, $\gamma = 45°$. This analysis reveals that the mutual inductance of an AUV wireless power transfer system is directly related to the relative position and posture of the coupling mechanism, with a change in any one of the selected parameters causing a change in the mutual inductance. However, the manner in which the mutual inductance is altered differs by parameter. In practical applications, adjusting a single parameter is insufficient to meet control requirements, and the system must be optimized globally. To achieve this, we establish a mutual inductance surrogate model in the following section.

Mutual inductance surrogate model and posture optimization of the coupling mechanism

As the measurement of mutual inductance during a dynamic process is very time-consuming, appropriate measuring equipment must be used. The relation between the relative position and posture of the primary and secondary coils and the transfer characteristics of the system is also extremely complicated, and the mutual inductance and transfer characteristics of the AUV wireless charging system LCC-S topology exhibits a positive correlation. To achieve global optimization of the mutual inductance parameters, we used a BP neural network to develop a mutual inductance surrogate model of the AUV wireless power transfer system that can predict the mutual inductance at any relative position and posture of the coupling mechanism. The Latin hypercube sampling method (LHS) was used to construct sample points for which the mutual inductance values were numerically simulated using the COMSOL software. Ten-fold cross-validation was used to avoid overfitting the surrogate model. The surrogate model developed in this section provides a model foundation for the posture optimization of the secondary coil under constant power transfer, as described in the next section. Other parameters of the coupling mechanism are listed in Table 2.
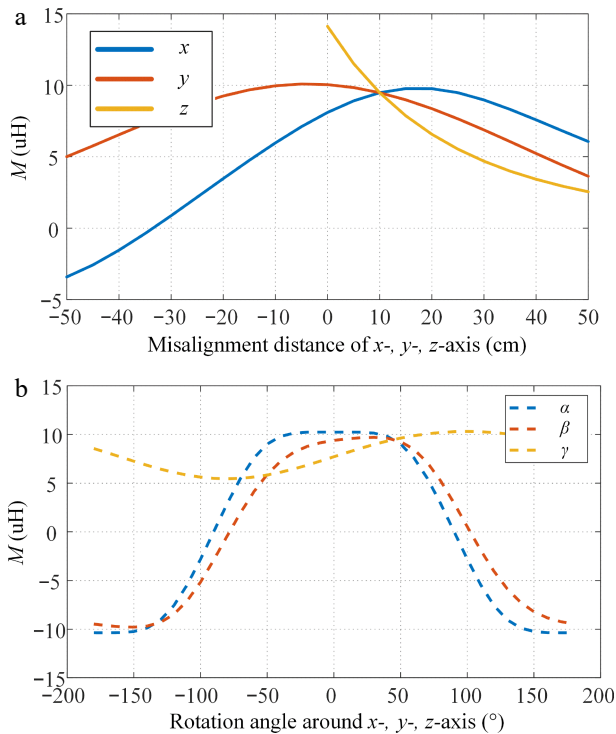
Numerical simulation and dataset creation

The LHS method was used to establish the sample space for the surrogate model. For each sampling point, the relative coordinates x, y, and z between the secondary and primary coils and the angles α, β, and γ of the secondary coil around the coordinate axis were selected as input variables and the mutual inductance of the coupling mechanism was selected as the output variable. LHS is an approximate random sampling method based on a multivariate parameter distribution and constitutes a stratified sampling technique with uniform stratification. LHS is able to construct models more effectively in sample spaces with high latitudes and low sample numbers. The ranges of all coupling parameters were defined based on the actual working area of the coupling coil, as shown in Table 3. A total of 10,000 sample points with different values of x, y, z, α, β, and γ were identified, 7,000 of which were used as the training set to determine the parameters of the surrogate model. The remaining 3,000 sample points were used as a test set to evaluate the predictive performance of the surrogate model. Using COMSOL software, a finite element model of each sample point was established and the electromagnetic field characteristics of the model were calculated, thereby obtaining the mutual inductance of the system.

Construction of mutual inductance surrogate model based on BP neural network

A multi-layer forward neural network based on error backpropagation was used to construct the surrogate model. As the activation function of a BP neural network is usually a sigmoid function that is continuously differentiable, any non-linear mapping between the input and output can be attained. Therefore, such networks are most extensively applied in pattern recognition, risk assessment, and adaptive control. The BP neural network design was initially researched and designed by Rumelhart et al.[34].

Figure 7 shows the architecture of a BP neural network. The main structure comprises an input layer, one or more hidden layers, and

Fig. 6 Mutual inductance M vs (a) misalignment distance, (b) rotational angle.

Table 2. Design parameters for coupling mechanisms in AUV UWPT systems.

Design parameters	Outer diameter	Inner diameter	No. of turns	No. of layers	Wire diameter
Primary coil	100 cm	60 cm	10	1	3.9 mm
Secondary coil	100 cm	60 cm	10	1	3.9 mm

Table 3. Range of variation in coupling parameters of AUV UWPT systems.

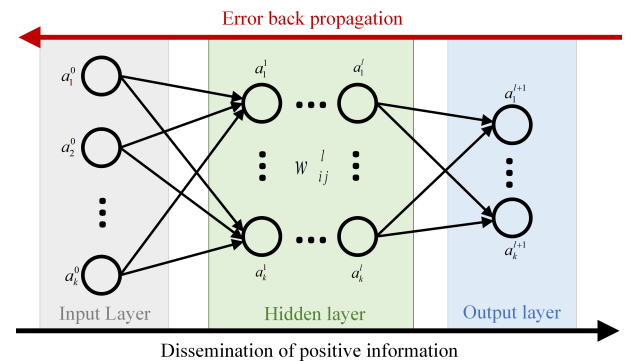| Coupling parameters	x (cm)	y (cm)	z (cm)	α (°)	β (°)	γ (°)
Data range	[−50.00, 50.00]	[−50.00, 50.00]	[50.00, 100.00]	[−90°, 90°]	[−90°, 90°]	[−90°, 90°]

Fig. 7 Neural network architecture.

an output layer. Each layer comprises several neurons, with the output of each neuron determined by its input value, effect function, and threshold value. In the figure, a_j^l represents the output of the j-th neuron in the l-th layer, w_{ij}^l represents the synaptic weight of the i-th neuron in the $(l-1)$-th layer to the j-th neuron in the l-th layer, b_j^l represents the deviation in the j-th neuron in the l-th layer, and σ represents the activation function. The output of the j-th neuron in the l-th layer can be given as:

$$a_j^l = \sigma(\sum_k w_{jk}^l a_k^{l-1} + b_j^l) \tag{11}$$

where L and α denote the loss function and learning rate, respectively, of the network. According to the gradient descent principle, the parameter update rule of the mutual inductance surrogate model can be given as:

$$\begin{cases} b^l \leftarrow b^l - \alpha \dfrac{\partial L}{\partial b^l} \\ w^l \leftarrow w^l - \alpha \dfrac{\partial L}{\partial w^l} \end{cases} \tag{12}$$

In building a BP neural network, all hyperparameters, including the learning rate, batch size, number of neurons, and number of hidden layers, must be fixed before model training begins. The performance of most machine learning models is largely determined by the choice of hyperparameters, with common hyperparameter optimization approaches used in current optimization methods including grid search, random search, and Bayesian optimization. As the principle of grid search is simple and suitable for cases with few hyperparameters, grid search was used to optimize the hyperparameters of the network.

Based on the theoretical analysis above, the number of neurons in the input and output layers were set as six and one, respectively, with the hyperparameters to be determined including the learning rate, activation function, batch size, number of neurons, and number of hidden layers. The Adam adaptive optimization algorithm[35] can be used to automatically adjust the learning rate. Although there is no approach in the existing literature providing a direct formula for adjusting the batch size, it has been proposed[36] that the optimal batch size lies within a range of 2 to 32. There is also no current theory for determining the optimal number of hidden layers and neurons required by a neural network to solve certain problems. In general, a neural network model with two to three hidden layers will have a sufficiently robust non-linear fitting ability to resolve most problems, and setting the same number of neurons in each hidden layer enables very good neural network

model performance. Based on the factors described above, the ranges of values of hyperparameters that needed to be determined *via* the grid search method are listed in Table 4.

The mean squared error (MSE), mean absolute error (MAE), and coefficient of determination (R^2) were used to evaluate the training performance and generalizability of the surrogate model using the following evaluation metrics:

$$MAE = \frac{1}{N} \sum_{i=1}^{N} |y_i - y_i'| \tag{13}$$

$$MSE = \frac{1}{N} \sum_{i=1}^{N} (y_i - y_i')^2 \tag{14}$$

$$R^2 = 1 - \sum_{i=1}^{N} (y_i - y_i')^2 \Big/ \sum_{i=1}^{N} (y_i - \bar{y})^2 \tag{15}$$

Table 5 lists the relative error of the neural network model that corresponds to each set of hyperparameters in the grid search after the same number of iterations, where HLN represents the number of hidden layers, NN represents the number of neurons in the hidden layer, BS represents the batch size, and R^2 represents the coefficient of determination between the predicted value of the model and the actual value. From Table 5, a network with two hidden layers, 32 neurons in each hidden layer, and a batch size of five achieves the best performance, with an R^2 of 0.9693.

Training of mutual inductance surrogate model

Using the dataset created previously, and the mutual inductance surrogate model established by the BP neural network algorithm, the relative position parameters (x, y, z) and posture parameters (α, β, γ) were set as input variables and the mutual inductance M was set as the output variable. The dataset of 10,000 sample points was divided into two subsets: one with 7,000 sample points to train and validate the surrogate model and another with 3,000 sample points to test the model. To obtain as much effective information as possible from the limited data and prevent overfitting of the surrogate model, a 10-fold cross-validation method was used to construct the surrogate model *via* the following steps:

Table 4. Search ranges of hyperparameters.

Hyperparameter	Search range
Number of hidden layers	2, 3, 4
Number of neurons in the hidden layer	16, 32, 64, 128
Batch size	4, 8, 16, 32

Table 5. R^2 values of surrogate models of different hyperparameter groups.

HLN	NN	BS	R^2	HLN	NN	BS	R^2	HLN	NN	BS	R^2
2	16	4	0.9552	3	16	4	0.9396	4	16	4	0.9665
2	16	8	0.8887	3	16	8	0.9584	4	16	8	0.9191
2	16	16	0.9519	3	16	16	0.9484	4	16	16	0.9247
2	16	32	0.9354	3	16	32	0.9492	4	16	32	0.9471
2	32	4	0.9693	3	32	4	0.9450	4	32	4	0.9395
2	32	8	0.9429	3	32	8	0.9621	4	32	8	0.9227
2	32	16	0.9256	3	32	16	0.8998	4	32	16	0.7922
2	32	32	0.9606	3	32	32	0.9060	4	32	32	0.8342
2	64	4	0.9372	3	64	4	0.9580	4	64	4	0.9365
2	64	8	0.9373	3	64	8	0.9645	4	64	8	0.9394
2	64	16	0.8674	3	64	16	0.8492	4	64	16	0.8663
2	64	32	0.9180	3	64	32	0.7726	4	64	32	0.7899
2	128	4	0.9581	3	128	4	0.9444	4	128	4	0.8855
2	128	8	0.8882	3	128	8	0.9446	4	128	8	0.9105
2	128	16	0.8045	3	128	16	0.9018	4	128	16	0.9630
2	128	32	0.8411	3	128	32	0.9550	4	128	32	0.9328

1) Divide the subset of 7,000 sample points into 10 groups, with each group including the same number of sample points randomly selected from the subset;

2) Construct 10 models. In the training and validation of each model, one group is selected as the validation dataset and the remaining nine are used as the training dataset. The model is trained using the training datasets and its R^2 value is calculated using the validation dataset;

3) The output of the 10 training models is averaged to give the output of the surrogate model.

The R^2 values of the 10 models in the validation dataset were 0.9045, 0.9619, 0.9620, 0.9610, 0.9551 0.9531, 0.9636, 0.9247, 0.9642, and 0.9591, respectively. The generalizability of the surrogate model was tested using the 3,000-sample-point test dataset. A comparison between the mutual inductance predicted by the surrogate model and that determined by the numerical simulation of the test dataset is shown in Fig. 8, with the convergence process of the surrogate model shown in Fig. 9. The R^2 value of the surrogate model was 0.9328, indicating that the model had robust generalizability. Using the surrogate model with the position parameters of the secondary coil relative to the primary coil in 3D space and posture parameters
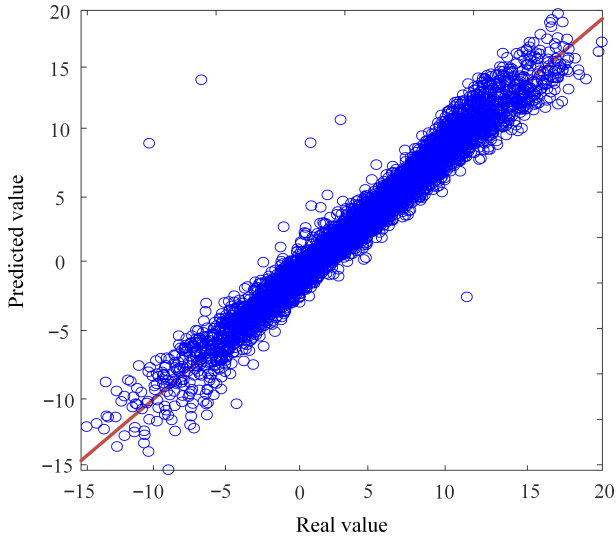

Fig. 8 Comparison between predicted and real mutual inductance values in the testing dataset.
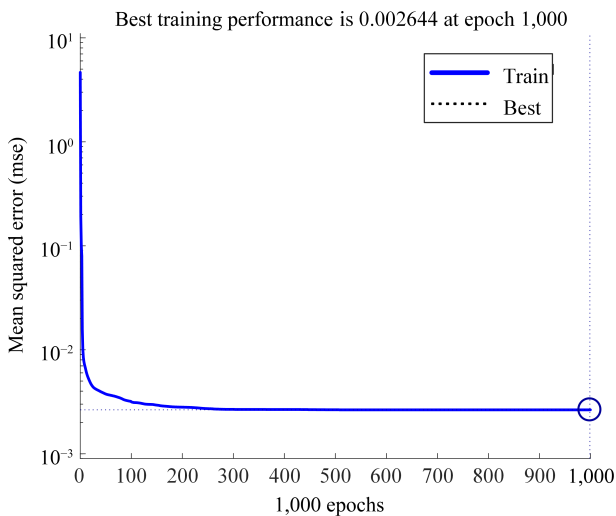

Fig. 9 Convergence process of the surrogate model.

of the secondary coil as inputs, the mutual inductance of the coupling mechanism can be determined quickly and effectively.

It was important to further verify the selected neural network regression algorithm, in particular in terms of its effectiveness and accuracy, to ensure that the constructed surrogate model provided the best performance in terms of model accuracy. After determining the hyperparameters of the neural network model, its accuracy was compared against those of commonly used regression algorithms for the construction of UWPT mutual inductance surrogate models, as shown in Table 6. It can be observed from the table that the R^2 value corresponding to the proposed neural network algorithm is the largest, indicating that its accuracy in constructing system energy efficiency models is significantly better than that of other regression algorithms.

Genetic algorithm for the posture optimization of coupling mechanisms with constant power transfer at misaligned positions

The surrogate model developed in the previous section can be used to quickly predict the mutual inductance of an AUV wireless power transfer system under different relative positions and postures. Here, we describe how a genetic algorithm, working with the surrogate model in an iterative process, can be applied in conditions in which the misaligned position is known to optimize the optimal posture of the secondary coil for constant power transfer at the misaligned position.

The genetic algorithm, an evolutionary computing technique proposed by John Holland and based on the law of evolution of organisms in nature, is a method for searching for an optimal solution by simulating natural evolutionary processes. The algorithm mathematically converts the problem-solving process into a process similar to the crossing over and mutation of chromosome genes in biological evolution. It is able to obtain better optimization results than conventional optimization algorithms in solving more complex combinatorial optimization problems. Owing to the complex relation between the optimized parameters of the relative position and posture and the objective function (coupled mutual inductance), the surrogate model constructed in the previous section allows for optimization with greater efficiency. The optimization process is shown in Fig. 10.

1) Randomly initialize the population: The individual coding is real-coded, with each individual constituting a real string composed of posture parameters (P, Q, R) of the coupling mechanism;

2) Determine the fitness function: To keep the mutual inductance in the misaligned state stable, the output of the mutual inductance surrogate model constructed, M_N, and the target mutual inductance value, M_0, are used to define the following fitness function:

$$F = e^{-|M_0 - M_N|} \tag{16}$$

3) Select operation: Select a number of individuals from the population as parents for breeding offspring and use the roulette wheel selection method to select operations. Individuals with high fitness have higher probabilities of passing their parameters to the next

Table 6. Comparison of accuracies of common regression algorithms for model building.

Regression algorithms	R^2
Polynomial regression	0.76
Support vector machine regression	0.65
K nearest neighbor regression	0.58
Random forest	0.74
BP neural network	0.93

generation; the converse is true for individuals with low fitness. The probability p_d of individual d being selected is:

$$p_d = \frac{F_d}{\sum_{d=1}^{h} F_d} \quad (17)$$

where, h is the number of individuals in the population and F_d indicates the fitness value of individual d;

4) Crossover operation: Two paired individuals exchange some of their genes with the crossover probability p, thus forming two new individuals. Using the real-valued crossover method, the crossover method of the t-th gene of individuals s_1 and s_2 can be represented as:

$$\begin{cases} g_{s_1 t} = g_{s_1 t} r + g_{s_2 t}(1-r) \\ g_{s_2 t} = g_{s_2 t} r + g_{s_1 t}(1-r) \end{cases} \quad (18)$$

where $g_{s_1 t}$ and $g_{s_2 t}$ represent the genes of the s_1-th and s_2-th individuals at the t-th position, respectively, and r is a random number between 0 and 1;

5) Mutation operation: To increase the diversity of the population, select the j-th gene g_{ij} of the i-th individual with a relatively small mutation probability p_s to mutate. The mutation operation method is as follows:

Through the optimization algorithm proposed in this section, the posture parameters of the coupling mechanism for constant power transfer in the misaligned position can be accurately obtained.

$$g_{ij} = \begin{cases} g_{ij} r_2 + (g_{ij} - g_{max}) r_1 (1 - s/s_{max}), & r_2 \geqslant 0.5 \\ g_{ij} r_2 + (g_{min} - g_{ij}) r_1 (1 - s/s_{max}), & r_2 < 0.5 \end{cases} \quad (19)$$
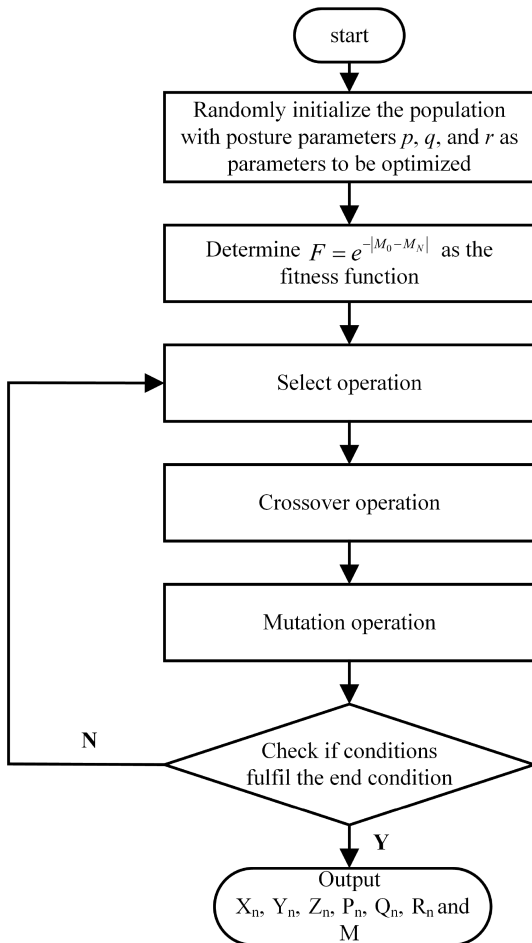

Fig. 10 Genetic algorithm optimization flow chart.

where g_{max} and g_{min} are the upper and lower bounds of gene g_{ij}, respectively, r_1 is a random number, s is the current iteration number, s_{max} is the maximum number of evolutions, and r_2 is a random number between 0 and 1;

6) Check if the fitness function value fulfills the end condition: If the condition is met, output the optimization result; otherwise proceed with the next iteration.

Through the optimization algorithm proposed in this section, the posture parameters of the coupling mechanism for constant power transfer in the misaligned position can be accurately obtained.

Verification of electromagnetic field simulation

To verify the accuracy of the algorithmic design and optimization process described in the previous section, in this chapter the optimization outcome of applying the algorithm to the lateral misalignment of the system when the distance-to-diameter ratio of the coupling mechanism is 0.6 is simulated. As the relative position parameters (x, y, z) of the primary and secondary coils during AUV wireless power transfer can be directly obtained from a sensor, the posture parameters (α, β, γ) of the secondary coil were optimized to maintain a constant mutual inductance at the misaligned position of the system. The reference point of the mutual inductance value when both coils are facing each other, $M_0 = 9.8265$ μH, was set as the algorithm's optimization target. Test points were taken along the misaligned path from one misaligned point (−50, 0, 60) to the other misaligned point (50, 0, 60) with a step length of 5 cm, resulting in a total of 21 test points to form the experimental set. The constant mutual inductance algorithm was optimized for the experimental set and the electromagnetic field simulation model was developed using the COMSOL finite element analysis software for simulation verification. The results of the optimization are shown in Fig. 11 below; the optimization results and raw error for each test point are listed in Table 7. Mutual inductance values before and after optimization of each test point in the experimental set are shown in Fig. 11.

From the figure, it is seen that the optimization algorithm can effectively achieve a constant mutual inductance value within the working range of the coupling mechanism with a misalignment distance of up to 25%. For the 11 sampling points, the average absolute and maximum absolute errors were 0.0426 and 0.0862 μH, respectively, and the average and maximum relative errors were 0.43% and 0.88%, respectively.

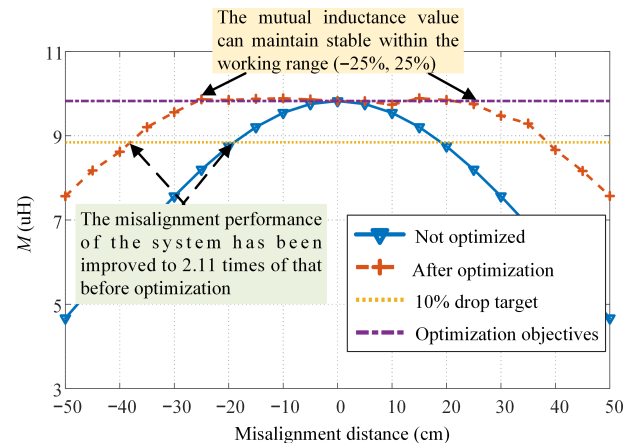Figure 12 shows convergence diagrams of the optimization

Fig. 11 Comparison of the mutual inductance of the system before and after optimization.

algorithm for each test point within the working range. At each test point, convergence was achieved within 20 iterations, demonstrating that the proposed algorithm can achieve good convergence to the optimal value over a small number of iterations, indicating that it is practical and can be applied in UWPT systems.

The posture and distribution of the magnetic field of the coupling mechanism at each misaligned point within the working range are shown in Fig. 13. When the misalignment distance exceeded 25%,

the mutual inductance could not be stabilized by adjusting the posture of the secondary coil, causing an inevitable drop in the mutual inductance. However, even in this extreme case the proposed optimization algorithm was still effective in significantly improving the mutual inductance, as shown in Fig. 14. When the mutual inductance dropped, the average mutual inductance of the system increased by 40.33%, with a maximum increase of 62.16%.

In practical applications, fluctuations in mutual inductance within

Table 7. Optimization results for each test point and error from the original data.

| Misalignment distance (cm)	Rotation angle p (around x-axis)	Rotation angle q (around y-axis)	Rotation angle r (around z-axis)	Mutual inductance without optimization algorithm (μH)	Mutual inductance with optimization algorithm (μH)	Optimized target of mutual inductance (μH)	Error (μH)
−50	86.44	−84.27	−85.64	4.6686	7.5662	9.8265	2.2603
−45	−89.42	49.9	89.83	5.4052	8.1761	9.8265	1.6504
−40	60.22	−59.56	−56.96	6.1473	8.6204	9.8265	1.2061
−35	73.18	45.05	−89.47	6.8746	9.2045	9.8265	0.622
−30	60.15	−35.85	−85.09	7.5657	9.5580	9.8265	0.2685
−25	33.10	−52.27	−51.11	8.1992	9.8658	9.8265	−0.0393
−20	−39.71	−36.58	16.72	8.7536	9.8517	9.8265	−0.0252
−15	−27.41	−31.49	−5.61	9.2086	9.8773	9.8265	−0.0508
−10	−33.45	−11.05	−6.70	9.5472	9.8895	9.8265	−0.063
−5	24.69	30.02	−1.25	9.7558	9.8636	9.8265	−0.0371
0	0	0	0	9.8265	9.8265	9.8265	0
5	17.83	−42.31	49.78	9.7559	9.8213	9.8265	0.0052
10	47.24	−10.61	20.01	9.5472	9.7403	9.8265	0.0862
15	−8.23	59.41	−49.73	9.2086	9.8909	9.8265	−0.0644
20	0.65	50.41	−34.48	8.7534	9.8502	9.8265	−0.0237
25	−3.67	60.82	−31.31	8.1994	9.7524	9.8265	0.0741
30	−58.25	35.81	−87.47	7.5658	9.4767	9.8265	0.3498
35	77.82	29.26	84.01	6.8745	9.2901	9.8265	0.5364
40	85.82	48.16	88.63	6.147	8.6633	9.8265	1.1632
45	89.99	41.02	89.99	5.4055	8.1647	9.8265	1.6618
50	89.99	48.85	89.99	4.6687	7.5706	9.8265	2.2559
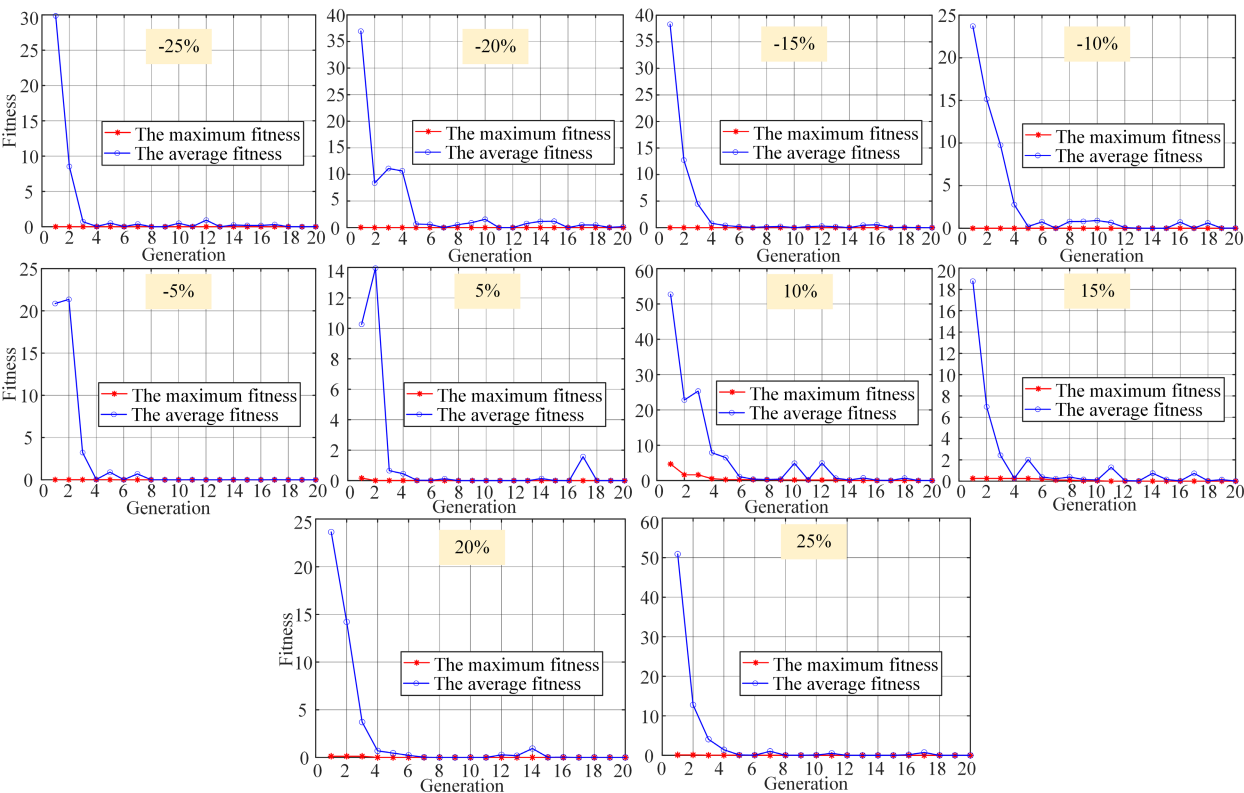
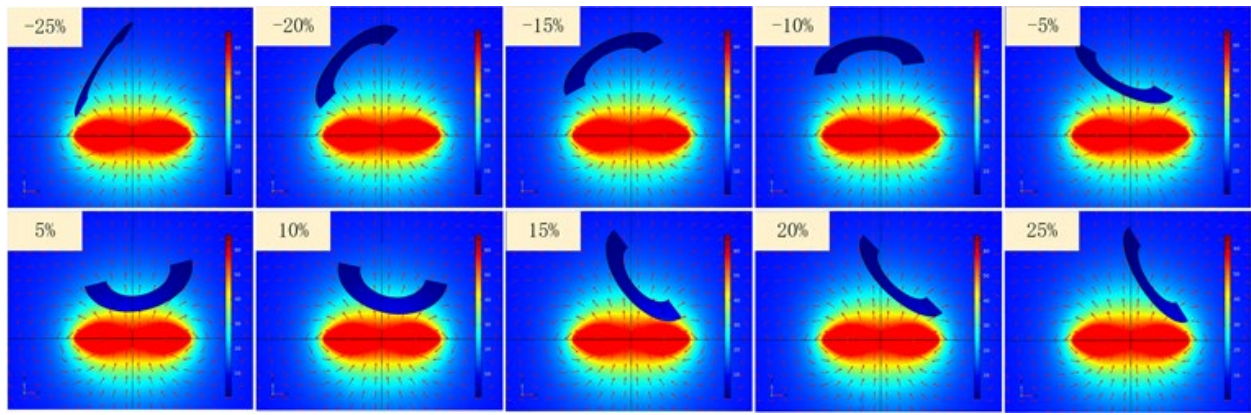**Fig. 12** Test set global optimization convergence process.

Fig. 13 Electromagnetic field simulation for each test point within the working range.
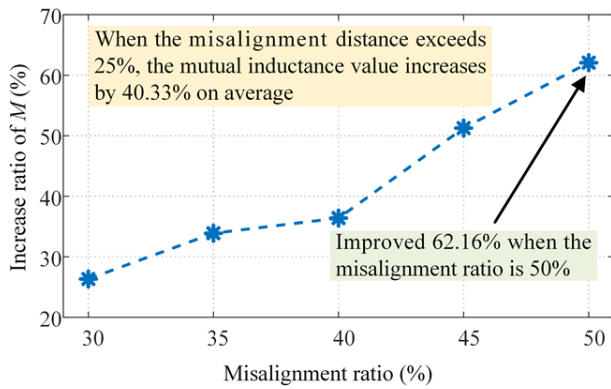

Fig. 14 Improvement of mutual inductance outside of the stable range by the optimization algorithm.

a range of 10% can be resolved *via* control methods. Under such conditions, as shown in Fig. 11, the anti-misalignment performance of the system increased by a factor of 2.11 relative to a case in which the secondary coil posture was not changed during misalignment, thereby effectively alleviating the impact of the drop in mutual inductance on the system's power transfer characteristics in the misaligned state.

Development and verification of the experimental platform

Development of the experimental platform

To further verify the practicality and accuracy of the algorithm design and optimization results, this section describes the experimental verification of the constant mutual inductance region of the mutual inductance curve of the experimental setup at a misalignment of between −25% and 25%. A 1 kW AUV wireless charging experimental prototype with LCC-S topology was established, as shown in Fig. 15. The full bridge inverter comprised four MOSFETs (NCEPOWER, NCE65T180F) driven by two half-bridge drivers (ST, L6387ED). The rectifier comprised four diodes (ONSEMI, MBR201000CT), and the main control chip adopted a complex programmable logic device (CPLD) (ALTERA, EPM240T100C5, with a crystal oscillator at 50 MHz). The system frequency, dead time, and system load were set to 152 kHz, 150 ns, and 20 Ω, respectively.

Verification of mutual inductance stability

From the theoretical analysis above, it was evident that mutual inductance would be a key factor in determining the power stability of the experimental system. Therefore, the stability of the mutual inductance was experimentally verified first. It was ensured that the primary and secondary coils were completely opposite, i.e., that the secondary coil had no misalignment or rotation and could serve as
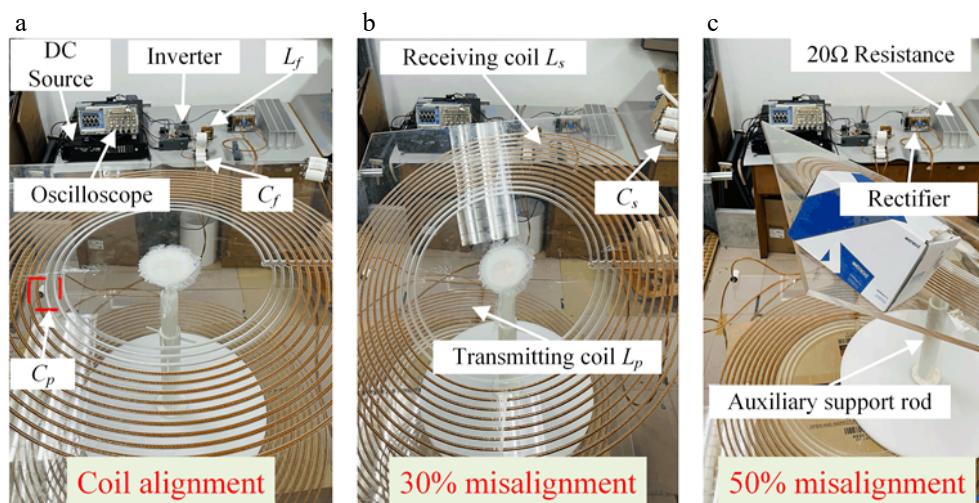

Fig. 15 Experimental prototype. (a) Coil alignment. (b) 30% misalignment. (c) 50% misalignment.

the reference point of the experiment. The secondary coil was also set as the optimization target of the experiment, with the mutual inductance value of the reference point measured as 10.7 µH. Furthermore, the simulation verification test points were used as the test points for the experimental verification and the misalignment pathway between the two misaligned points [(−50,0,60) and (50,0,60), respectively] was sampled with a step size of 5 cm. The measured mutual inductance values of each test point before and after optimization by the algorithm are shown in Fig. 16.

Evidently, using the algorithm, the mutual inductance value of the coupling mechanism could be stabilized by adjusting the posture of the secondary coil within the working range (−25%, 25%) with an average error of 4.2%. The mutual inductance of the system also significantly improved beyond the working range, with a maximum increase of 63.9%, a result consistent with the simulation results.

Verification of power stability

To further verify the practicality of the proposed algorithm, a power experiment was performed on the experimental system at test points within the working range, with the different cases of resulting power transfer shown in Fig. 17. When the coupling mechanism was aligned, the power transfer of the system was 1,155.2 W with an efficiency of 91.2%. When the system was misaligned by 25%, the optimizing algorithm maintained the mutual inductance at around 10.6 µH with a system efficiency of 90.8%. Using the method proposed in this paper, the waveforms of the current and voltage of the system in misalignment situations were fundamentally unchanged, thereby confirming power stability. Furthermore, soft switching was attained over the full range of misalignment to ensure the safe and efficient operation of the system, maintaining

the system efficiency at approximately 90%.

Based on the power curve in Fig. 18, it is evident that the optimized system can perform a constant power transfer of 1.15 kW in the misaligned state. The overall efficiency of the system reached 91% and the average power transfer of the system increased by 18.91%, with a maximum increase of 48.16%. There was some deviation between the experimental and simulation reference points, primarily the result of deviations in the measurement of the experimental environment and system parameters. However, as the relative errors of the experiment were very small, the optimization algorithm proposed in this paper was shown to be accurate and effective.

Conclusions

This paper proposed an optimal misalignment posture prediction algorithm for coupling mechanisms based on the mutual inductance surrogate model. The algorithm predicts the optimal posture for constant power transfer in the misaligned state of a coupling mechanism within its working range by adjusting the posture of the secondary coupling mechanism. The simulation and experimental results reported in this paper indicate that the proposed algorithm can achieve constant mutual inductance, thereby ensuring constant power transfer. Unlike existing anti-misalignment solutions used by the wireless power transfer systems of AUV, the proposed algorithm avoids issues with docking and reduces the structural complexities of the wireless charging coupling mechanism, enabling dynamic wireless charging underwater and significantly enhancing flexibility and practicality.

The strengths and significance of the research reported in this paper can be enumerated as follows: (1) The constructed surrogate
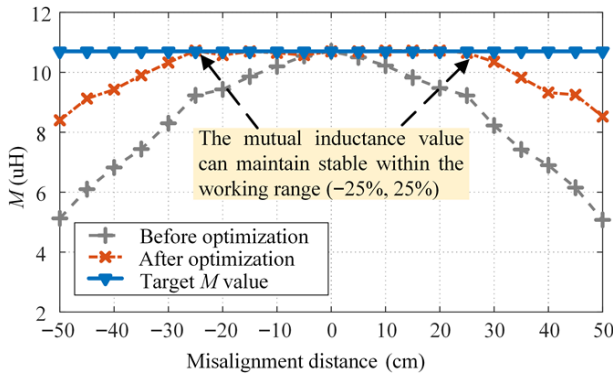
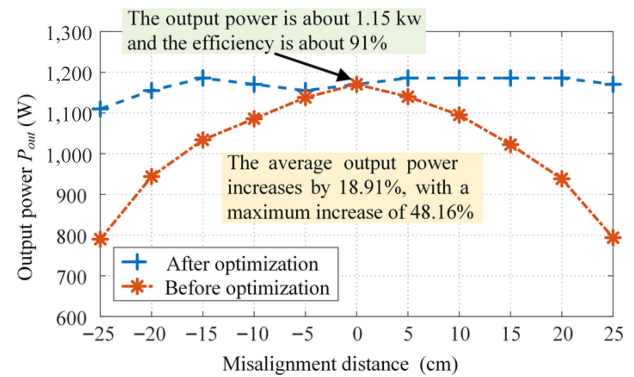

Fig. 16 Comparison curve for mutual inductance M.

Fig. 18 Comparison curve for output power P_{out}.
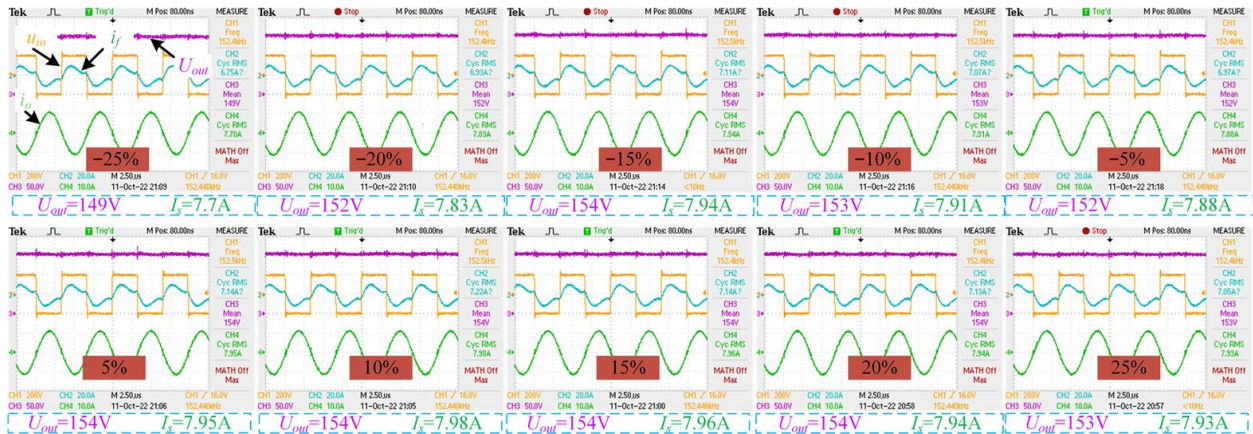

Fig. 17 Experimental waveforms for different misalignment cases with the proposed algorithm adopted.

model can accurately derive the mutual inductance value of a coupling mechanism at any position and posture. (2) The optimization algorithm proposed in this paper can effectively achieve a constant mutual inductance value in a coupling mechanism in the misaligned state in 3D space, thereby achieving stable power transfer. (3) The method proposed in this paper can be adapted to other fields and is not limited by the elements constituting the coupling mechanism in terms of shape, material, or the presence or absence of a magnetic core. The experimental prototype was built to verify the practicality of the proposed method revealed that the system can guarantee a constant mutual inductance within a 25% misalignment range and an aspect ratio of 0.6 with an average error of only 4.2%. When the mutual inductance falls within 10%, the anti-misalignment range of the system is increased to 2.11 times that before optimization.

Author contributions

The roles and contributions to the paper of each author are described as follows: Study conception and design: Feng Y, Sun Y; data collection: Feng Y, Lin T, Chen F; analysis and interpretation of results: Feng Y, Hu H; draft manuscript preparation: Feng Y. All authors reviewed the results and approved the final version of the manuscript.

Data availability

All data included in this study are available upon request by contact with the corresponding author.

Acknowledgments

Conflict of interest

The authors declare that they have no conflict of interest.

Dates

References

1. Nguyen HT, Alsawalhi JY, Al Hosani K, Al-Sumaiti AS, Ali Al Jaafari K, et al. 2022. Review map of comparative designs for wireless high-power transfer systems in EV applications: maximum efficiency, ZPA, and CC/CV modes at fixed resonance frequency independent from coupling coefficient. *IEEE Transactions on Power Electronics* 37(4):4857−76

2. Fan Y, Sun Y, Dai X, Zuo Z, You A. 2021. Simultaneous wireless power transfer and full-duplex communication with a single coupling interface. *IEEE Transactions on Power Electronics* 36(6):6313−22

3. Zhang Z, Pang H, Georgiadis A, Cecati C. 2019. Wireless power transfer—an overview. *IEEE Transactions on Industrial Electronics* 66(2):1044−58

4. Roy S, Azad ANMW, Baidya S, Alam MK, Khan F. 2022. Powering solutions for biomedical sensors and implants inside the human body: a comprehensive review on energy harvesting units, energy storage, and wireless power transfer techniques. *IEEE Transactions on Power Electronics* 37(10):12237−63

5. Liu Z, Su YG, Zhao YM, Hu AP, Dai X. 2022. Capacitive power transfer system with double T-type resonant network for mobile devices charging/supply. *IEEE Transactions on Power Electronics,* 37(2):2394−403

6. Painter H, Flynn J. 2006. Current and future wet-mate connector technology developments for scientific seabed observatory applications. *Proceeding OCEANS 2006, Boston, MA, USA, 18–21 September 2006.* pp. 1–6. https://doi.org/10.1109/OCEANS.2006.306829

7. Covic GA, Boys JT. 2013. Modern trends in inductive power transfer for transportation applications. *IEEE Journal of Emerging and Selected Topics in Power Electronics* 1(1):28−41

8. Teeneti CR, Truscott TT, Beal DN, Pantic Z. 2021. Review of Wireless Charging Systems for Autonomous Underwater Vehicles. *IEEE Journal of Oceanic Engineering* 46(1):68−87

9. Singh H, Bellingham JG, Hover F, Lemer S, Moran BA, et al. 2001. Docking for an autonomous ocean sampling network. *IEEE Journal of Oceanic Engineering* 26(4):498−514

10. Coulson R, Lambiotte JC, Grenon G, Pantelakis T, Curran J, et al. 2004. Development of a modular docking sub-system for 12 class autonomous underwater vehicles. *Oceans '04 MTS/IEEE Techno-Ocean '04 (IEEE Cat. No.04CH37600), Kobe, Japan, 9–12 November 2004.* vol 3. pp. 1745–49. https://doi.org/10.1109/OCEANS.2004.1406388

11. Shizuno K, Yoshida S, Tanomura M, Hama Y. 2014. Long distance high efficient underwater wireless charging system using dielectric-assist antenna. *Proceeding 2014 Oceans, St. John's, NL, Canada, 14–19 September 2014.* pp. 1–3. https://doi.org/10.1109/OCEANS.2014.7002986

12. Yoshida S, Tanomura M, Hama Y, Hirose T, Suzuki A, et al. 2016. Underwater wireless power transfer for non-fixed unmanned underwater vehicle in the ocean. *2016 IEEE/OES Autonomous Underwater Vehicles (AUV), Tokyo, Japan, 6–9 November 2016.* pp. 177–80. https://doi.org/10.1109/AUV.2016.7778668

13. Urano M, Ata K, Takahashi A. 2016. Study on underwater wireless power transfer via electric coupling with a submerged electrode. *2017 IEEE International Meeting for Future of Electron Devices, Kansai (IMFEDK), Kyoto, Japan, 29–30 June 2017* pp. 36–37. https://doi.org/10.1109/IMFEDK.2017.7998030

14. Feezor MD, Yates Sorrell S, Blankinship PD. 2001. An interface system for autonomous undersea vehicles. *IEEE Journal of Oceanic Engineering* 26(4):522−25

15. Orekan T, Zhang P. 2019. Study and Analysis of Underwater Wireless Power Transfer. In *Underwater wireless power transfer: smart ocean energy converters.* Cham: Springer. pp 35–49. https://doi.org/10.1007/978-3-030-02562-5_3

16. Assaf T, Stefanini C, Dario P. 2013. Autonomous underwater biorobots: A wireless system for power transfer. *IEEE Robotics & Automation Magazine* 20(3):26−32

17. Cai C, Wu S, Zhang Z, Jiang L, Yang. 2021. Development of a fit-to-surface and lightweight magnetic coupler for autonomous underwater vehicle wireless charging systems. *IEEE Transactions on Power Electronics* 36(9):9927−40

18. Liu S, Su J, Lai J, Zhang J, Xu H. 2021. Precise modeling of mutual inductance for planar spiral coils in wireless power transfer and its application. *IEEE Transactions on Power Electronics* 36(9):9876−85

19. Delgado A, Requena NA, Ramos R, Oliver JA, Alou P, et al. 2020. Design of inductive power transfer system with a behavior of voltage source in open-loop considering wide mutual inductance variation. *IEEE Transactions on Power Electronics* 35(11):11453−62

20. Liu F, Yang Y, Jiang D, Ruan X, Chen X. 2017. Modeling and optimization of magnetically coupled resonant wireless power transfer system with varying spatial scales. *IEEE Transactions on Power Electronics* 32(4):3240−50

21. Shin Y, Woo S, Rhee J, Lee C, Kim H, et al. 2022. Accurate method for extracting the coupling coefficient of an LCC-series wireless power transfer system. *IEEE Transactions on Power Electronics* 37(9):11406−22

22. Cha HR, Park KR, Kim TJ, Kim RY. 2021. Design of magnetic structure for omnidirectional wireless power transfer. *IEEE Transactions on Power Electronics* 36(8):8849−60

23. Yin J, Lin D, Parisini T, Hui S. 2016. Front-End Monitoring of the Mutual Inductance and Load Resistance in a Series–Series Compensated Wireless Power Transfer System. *IEEE Transactions on Power Electronics* 31(10):7339−52

24. Wang L, Sun P, Wu X, Cai J, Deng Q, et al. 2022. Mutual Inductance Identification of IPT System Based on Soft-Start Process. *IEEE Transactions on Power Electronics* 37(6):7504−17

25. Yan Z, Zhang Y, Kan T, Lu F, Zhang K, et a. 2019. Frequency optimization of a loosely coupled underwater wireless power transfer system considering eddy current loss. *Transactions on Industrial Electronics* 66(5):3468−76

26. Yan Z, Song B, Zhang Y, Zhang K, Mao Z, et al. 2019. A rotation-free wireless power transfer system with stable output power and efficiency for autonomous underwater vehicles. *IEEE Transactions on Power Electronics* 34(5):4005−8

27. Yan Z, Zhang Y, Zhang K, Song B, Mi C. 2019. Underwater wireless power transfer system with a curly coil structure for auvs. *IET Power Electronics* 12(10):2559−2565

28. Cheng Z, Lei Y, Song K, Zhu C. 2015. Design and loss analysis of loosely coupled transformer for an underwater high-power inductive power transfer system. *IEEE Transactions on Magnetics* 51(7):8401110

29. Zhou J, Yao P, Chen Y, Guo K, Hu S, et al. 2021. Design considerations for a self-latching coupling structure of inductive power transfer for autonomous underwater vehicle. *IEEE Transactions on Industry Applications* 57(1):580−87

30. Feng T, Zuo Z, Sun Y, Dai X, Wu X, et al. 2022. A reticulated planar transmitter using a three-dimensional rotating magnetic field for free-positioning omnidirectional wireless power transfer. *IEEE Transactions on Power Electronics* 37(8):9999−10015

31. Zhao L, Thrimawithana DJ, Madawala UK. 2017. Hybrid bidirectional wireless EV charging system tolerant to pad misalignment. *IEEE Transactions on Industrial Electronics* 64(9):7079−7086

32. Zhao L, Thrimawithana DJ, Madawala UK, Hu AP, Mi CC. 2019. A misalignment-tolerant series-hybrid wireless EV charging system with integrated magnetics. *IEEE Transactions on Power Electronics* 34(2):1276−85

33. Ramegowda M. 2014. *Classical mechanics. Govt. College (Auton.), Mandya, 2014*. www.gcm.ac.in/downloads/elearning/Classical_Physics_s3.pdf

34. Rumelhart DE, Hinton GE, Williams RJ. 1986. Learning representations by back propagating errors. *Nature* 323:533−36

35. Bui DT, Hoang ND, Martínez-Álvarez F, Thao NTP, Hoa PV, et al. 2019. A novel deep learning neural network approach for predicting flash flood susceptibility: A case study at a high frequency tropical storm area. *Science of The Total Environment* 701:134413

36. Kingma D, Ba J. 2015. A method for stochastic optimization. *Proceedings of the International Conference on Learning Representations, San Diego, 2015*. https://doi.org/10.48550/arXiv.1412.6980